

Automatic 3D Modelling for Microweather-Informed Advanced Air Mobility Planning and Optimisation

E. Aldao¹, F. Veiga-López¹, G. Veiga-Piñeiro², P. Domínguez-Estévez², G. Fontenla-Carrera¹, E. Martín² and H. González-Jorge¹

¹Aerolab, Instituto de Física e Ciencias Aeroespaciais (IFCAE), Universidade de Vigo, Campus de As Lagoas, Ourense, E-32004, Spain

²Chemical, Thermal, and Environmental Engineering Group, Instituto de Física e Ciencias Aeroespaciais (IFCAE), Universidade de Vigo, Campus de As Lagoas, Ourense, E-32004, Spain

enrique.aldao.pensado@uvigo.gal

Abstract

Meteorological phenomena, such as shear and wind gusts, pose a significant risk to the safety and efficiency of Advanced Air Mobility operations. In urban and interurban environments, wind dynamics are influenced by the interaction with buildings and terrain, resulting in small-scale phenomena such as boundary layer detachments, turbulence, or wind gusts. These fluctuations in wind speed and pressure pose a challenge for the safe implementation of Urban Air Mobility operations, as they generate unsteady forces that can destabilise the flight of small aircraft. To predict these phenomena, which typically occur at a scale of a few meters and even centimetres, high-resolution Computational Fluid Dynamics (CFD) models are required as current meteorological prediction tools lack sufficient resolution. For a fair implementation of the CFD analysis, detailed models of the study area are required. These include the local geometry (including geographical topology, buildings, etc.) and the correct characterisation of surface properties such as roughness and thermal conductivity, being the latter critical for the correct modelling of the dissipation of viscous energy and heat exchange between the wind and the terrain. However, many public 3D geometric datasets lack these interesting surface properties, as most are oriented towards visualisation purposes. Moreover, geometrical errors are frequently present in this kind of datasets, such as non-manifold edges or gaps that can impede the automatic generation of the CFD computational domain. This work introduces an automated methodology for the development of interurban CFD meshes for the design and optimisation of Advanced Air Mobility operations. Using open-source databases provided by the National Geographic Institute (IGN) of Spain, a semantically characterised geometric model of an interurban area on the outskirts of the city of Vigo (Spain) was developed. This geometry was employed to obtain the computational domain compatible with the open-source CFD software OpenFOAM. Furthermore, simulations were carried out to analyse the formation of wind gusts in the area. For this purpose, several flight conditions of UAVs (Unmanned Aerial Vehicles) were simulated, and the fluctuations in wind speed were recreated using a Dryden model adjusted from the turbulence parameters of CFD results. Results showed that areas with significant changes in elevation are prone to the formation of wakes and high-intensity turbulence, compromising the safety of AAM operations. This phenomenon is particularly relevant in flights close to ground level, where high-frequency velocity field fluctuations appear.

1 Introduction

Advanced Air Mobility (AAM) is an emerging sector of transportation that seeks to move people and goods in interurban areas through various aerial platforms available in the market [1, 2]. Within the concept of AAM, different types of aircraft are encompassed, such as traditional helicopters, VTOL (Vertical Take-off and Landing) aircraft, and UAVs (Unmanned Aerial Vehicles) integrated into the same airspace [3, 4]. This convergence of aerial technologies offers versatile solutions to mitigate ground traffic congestion, reduce travel times, and improve connectivity in metropolitan areas [5, 6, 7].

The implementation of these services will take place gradually, overcoming technological, ethical, and legal challenges to ensure the safety of operations. This process involves careful considerations, such as integration

with current air traffic, aircraft certification, and the management of contingencies due to external factors such as atmospheric turbulence and wind gusts [8, 9, 10]. In both urban and interurban environments, these phenomena arise due to the interaction of wind with terrain and buildings generating complex wind patterns with unsteady changes in pressure and wind speed. These disturbances may cause disruptions in AAM services, leading to potential delays, cancellations, and reduced airspace capacity [11, 12].

In order to mitigate the effects of meteorology, monitoring systems are crucial for predicting the atmospheric flows. According to the AAM Concept of Operations by NASA (National Aeronautics and Space Administration), these services would be overseen by Weather Supplemental Data Service Providers (SDSPs), equipped with real-time data acquisition systems based on ground observation stations and sensors embedded in aircraft. In addition to observation capabilities, high-resolution Numerical Weather Prediction (NWP) products such as Computational Fluid Dynamics (CFD) models are required to analyse the acquired data and generate accurate predictions for interurban atmospheric conditions [13, 14].

These numerical products simulate the atmospheric flow behaviour by solving the Navier-Stokes equations within a high-resolution computational domain of the study environment. This allows for the resolution of small-scale phenomena such as gust formation, flow instabilities, or boundary layer detachments [15, 16]. Traditionally, the main drawback of these tools has always been their high computational cost, typically on the order of several hours per simulation [17, 18, 19], which limited their applicability to real-time systems. However, with the introduction of Reduced Order Models (ROMs), it is now possible to make real-time predictions based on simulation databases with different boundary conditions [20, 21, 22].

Despite these advances, the development of CFD systems requires detailed models of the simulation environment, encompassing both the geometry and the physical properties of the surfaces such as roughness and thermal conductivity. However, most of public 3D model databases are oriented towards visualisation and animation purposes and they do not provide information about surface properties [23, 24, 25]. Furthermore, as these models are typically obtained using photogrammetry techniques or LiDAR point clouds, they can contain errors in the geometry such as missing surfaces, self-intersections, and non-manifold edges [26, 27]. Correcting these errors is a time-consuming process involving multiple hours of surface processing and manual work, which may not be feasible in many applications [28].

As the main contribution of this work, we present a methodology for the development of CFD interurban meteorological prediction systems using open-source data. The developed tool automatically generates finite volume meshes compatible with the open-source software OpenFOAM, semantically characterised by the properties of different terrain surfaces. With this approach, the wind patterns of an interurban area are simulated and an analysis is carried out to determine the areas susceptible to turbulence formation.

The remainder of the manuscript is structured as follows: Section 2 presents the methodology, introducing the open-source data inputs as well as the automatic geometric modelling of the urban area. In Section 3, the results are discussed and analysed. Finally, the main conclusions of this work are included in Section 4.

2 Methodology

As a practical case study, we consider an area on the outskirts of Vigo, a city of about 300,000 inhabitants located in the northwest of Spain (Figure 1). This area houses the main hospital of the city, which in the future could serve as a logistical centre for AAM operations such as the urgent delivery of medical equipment or air ambulances. However, the area features terrain with significant slopes and mountains that contribute to the formation of turbulence and wind gusts, posing a risk to the safety of operations.

2.1 Terrain geometric modelling

To generate the environment 3D model, we firstly employ the digital terrain model of the area depicted in Figure 2(a). These data, provided by the National Geographic Institute (IGN) of Spain [29], consist of a regularly spaced grid with a resolution of 25 metres, mapping the elevation relative to sea level. With this raster information, a Delaunay triangulation is applied to obtain the 3D mesh of terrain represented in Figure 2(b).

This mesh features significant slopes at the boundaries of the study case domain, with elevation values ranging between 0 and 500 metres. Therefore, to avoid numerical instabilities in the CFD model, an entrance channel is added to the domain boundaries. This external surface consists of two parts, as shown in Figure 3.

1. *Constant Height Plane*: A completely flat area with a constant elevation equal to the median height at the boundaries of the terrain. As this surface is horizontal, it ensures a clean and organised inflow and outflow. It covers an extension of 250 metres, starting from the outer boundary of the transition area.

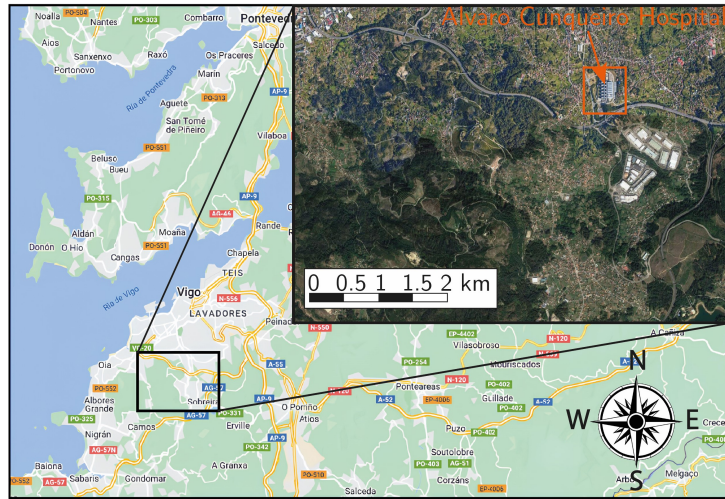


Figure 1: Area of study.

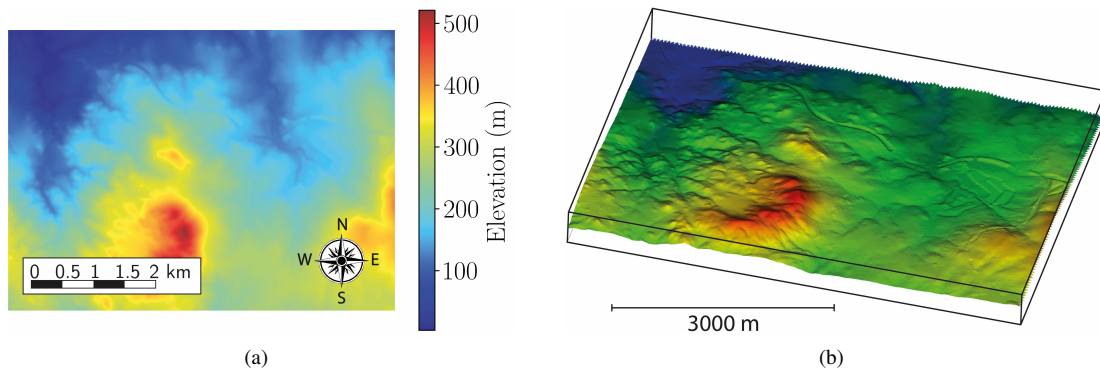


Figure 2: Geometric model generation. a) Digital Terrain Model of the area. b) Terrain 3D mesh.

2. *Transition Area*: It extends from the limits of the terrain mesh to the Constant Height Plane. It spans 750 metres so as to avoid abrupt height variations that may cause flow instabilities. To this end, a linear interpolation is applied between the terrain mesh and the outer plane.

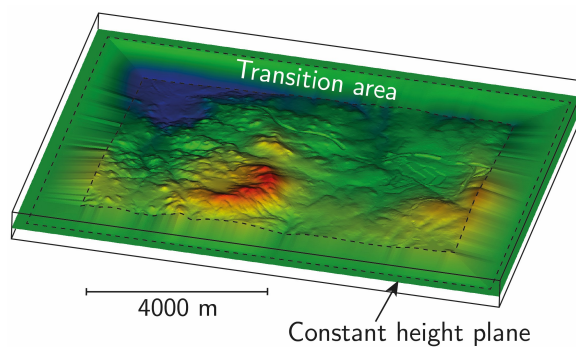


Figure 3: SIOSE AR Semantic Classification Model.

2.2 Terrain semantic classification

To characterise the physical properties of terrain surfaces, we utilise the SIOSE AR model from IGN [30]. This product is a high-resolution semantic classification model that characterises the surfaces of Spanish territory (Figure 4). It was elaborated combining multiple sources of information such as aerial LiDAR point clouds, aerial imagery, cadastral data and farmers' declarations.

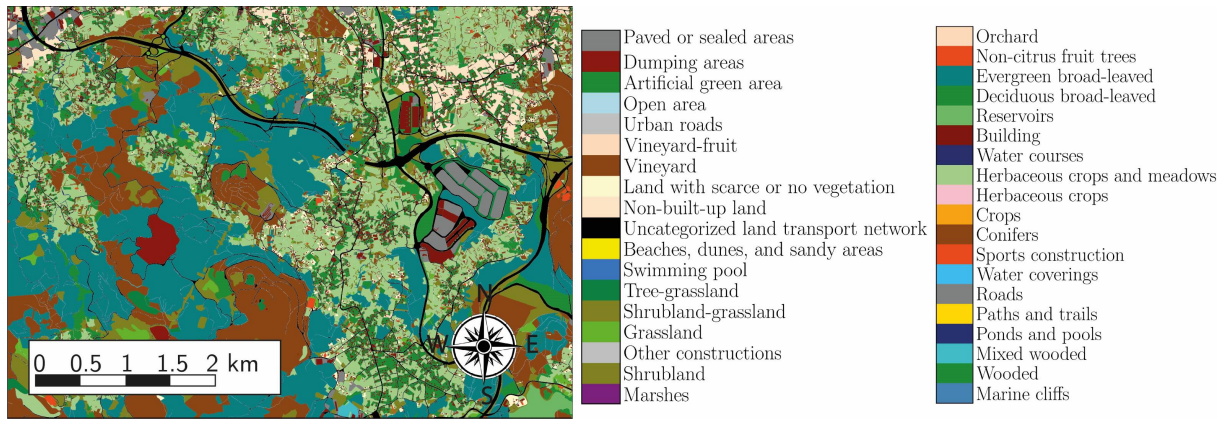


Figure 4: SIOSE AR Semantic Classification Model.

With this product, the triangles of the terrain mesh are assigned the SIOSE AR category of their centroids, providing the semantically classified mesh depicted in Figure 5. This procedure is only applied to the triangles of terrain geometry. The entrance channel is not labelled, as it is an artificial extension of the computational domain to improve the stability of simulations.

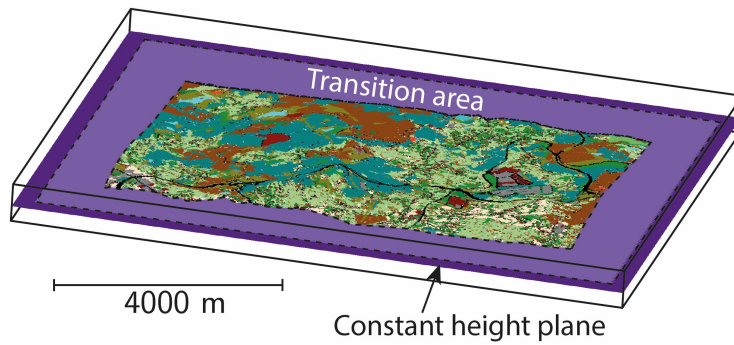


Figure 5: Semantically classified 3D mesh.

2.3 Computational domain mesh generation

The computational domain is created using Ansys Workbench modelling software. Firstly, a rectangular parallelepiped, ranging from 0 to 1250 metres above sea level, is generated to cover the terrain mesh depicted in Figure 5. Subsequently, a boolean operation is executed to eliminate the volume below the terrain surface, resulting in the computational domain depicted in Figure 6.

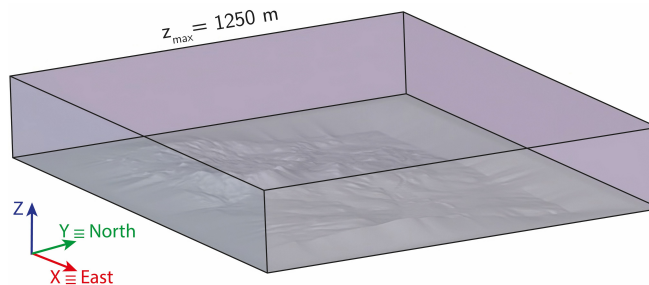


Figure 6: Computational domain.

Finally, the mesh is computed with a hybrid meshing method encompassing hexahedral, tetrahedral, and octahedral elements. This method, ensures a robust and precise fit to the terrain surfaces, while providing a high level of orthogonality and aspect ratios close to one. In the proximities of terrain, local refinements are implemented to achieve low values of y_+ and resolve the effects of boundary layer viscous dissipation. This procedure

is performed iteratively, until obtaining suitable values for the conditions of the problem. After this process, a final mesh, composed of 46.5 million cells, is obtained.

2.4 CFD simulation setup

The wind profiles are calculated using the simpleFoam solver from OpenFOAM, an open-source solver designed for incompressible and steady flows. The $k - \varepsilon$ turbulence model is used to replicate the turbulence energy dissipation effects. This RANS model employs two equations to consider the turbulence's impact on mean flow properties. One equation models turbulence kinetic energy; and the other the rate of dissipation of turbulence kinetic energy (ε). This method features a good balance between computational cost and precision for large scale simulations as in this work. It is noteworthy that, given the complexity of terrain's geometry, opting for a more detailed method is strongly discouraged as it would lead to unfeasible computational costs.

To establish the boundary conditions, we consulted the Meteogalicia website, the main meteorological agency in the region [31]. Based on Meteogalicia's data, the prevailing wind direction is 180 degrees, indicating south winds. Consequently, the south face of the computational domain is designated as the inlet, where ABL (Atmospheric Boundary Layer) conditions with are defined. The opposite is set as the outlet, with fixed atmospheric pressure. Symmetry conditions are applied to the lateral and upper faces, while in the ground surface, a wall model is applied employing a nutk wall function with variable roughness parameters. Figure 7 presents a scheme of the boundary conditions of the problem.

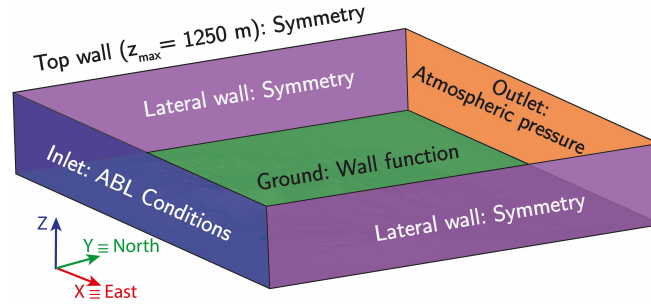


Figure 7: Boundary conditions.

Table 1 presents the roughness lengths employed in the nutk wall function for the different categories of SIOSE AR. These values are assigned based on the results of an article of Silva et al., in which they characterised the properties of different terrain surfaces [32].

Table 1: Terrain roughness length values.

Category	Roughness (m)
Mixed wooded, Wooded, Conifers, Tree-grassland, Evergreen broad-leaved, Deciduous broad-leaved	0.7
Crops, Herbaceous crops, Herbaceous crops and meadows, Orchard, Marshes, Shrubland, Grassland	0.1
Land with scarce or no vegetation, Open area, Non-built-up land, Reservoirs, Swimming pool, Water coverings, Beaches, dunes, and sandy areas, Ponds and pools, Dumping areas, Marine cliffs	0.05
Building, Sports construction, Other constructions	0.5
Paths and trails, Uncategorised land transport network, Urban roads, Paved or sealed areas	0.075
Transition area, Constant height plane	0.1

2.5 Turbulence simulation

With the results of CFD simulations, a Dryden turbulence model is adjusted to assess the formation of wind gusts. This model replicates the variations in the components of True Airspeed in the aircraft reference frame (u_g, v_g, w_g) as a stochastic process characterised by the Power Spectral Densities defined as

$$\Phi_{u_g}(\Omega) = \sigma_u^2 \frac{2L_u}{\pi} \frac{1}{1 + (L_u\Omega)^2} ; \Phi_{v_g}(\Omega) = \sigma_v^2 \frac{2L_v}{\pi} \frac{1 + 12(L_v\Omega)^2}{1 + (L_v\Omega)^2} ; \Phi_{w_g}(\Omega) = \sigma_w^2 \frac{2L_w}{\pi} \frac{1 + 12(L_w\Omega)^2}{1 + (L_w\Omega)^2}, \quad (1)$$

where:

- Ω is a spatial frequency equal to the ratio between the angular rate w and the modulus of the True Airspeed v_{TAS} .
- $\sigma_u, \sigma_v, \sigma_w$ are the turbulence intensities for the three velocity components.
- L_u, L_v, L_w represent the scale length for each direction.

The values of turbulence intensities and scale lengths are computed using the variables of the $k - \epsilon$ model, assuming the turbulence properties are isotropic. With this simplification, their values can be obtained using

$$\sigma_u = \sigma_v = \sigma_w = \sqrt{\frac{2k}{3}} ; \quad L_u = L_v = L_w = C_\mu^{0.75} \frac{k^{1.5}}{\epsilon}, \quad (2)$$

where C_μ is a model constant equal to 0.09. In this way, the atmospheric turbulence is modelled performing random sampling of the PSD (Power Spectral Density) functions adjusted with CFD results. For this purpose, results from a previous work of Abichandani et al. were utilised [33].

3 Results

3.1 CFD Results

Figures 8 and 9 represent the results of kinetic turbulence energy (k) and the rate of dissipation of turbulent kinetic energy (ϵ) for an input friction velocity v^* of 3 m/s. This parameter represents the mean velocity at a characteristic height of the logarithmic profile of the ABL (Atmospheric Boundary Layer) boundary conditions. High values of this parameter indicate atmospheric conditions with high wind intensity.

As can be seen, the values of k and ϵ are very close to zero in all zones of the domain. This is due to the low velocity of the incoming flow, which lacks sufficient kinetic energy to create zones of high turbulence intensity. Additionally, Figure 9 presents the wind velocity map through wind barbs. Long lines on a wind symbol indicate its direction. The short transverse barbs represent the intensity: each half-line is 5 knots, and a full line is 10 knots. The sum of these transverse lines gives the total wind speed at that location.

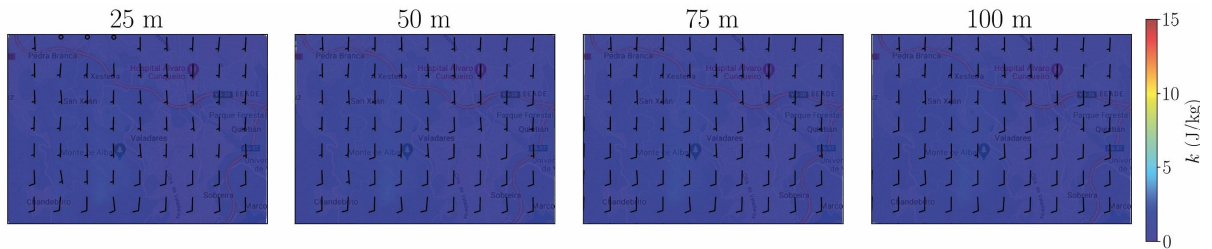


Figure 8: Kinetic turbulence energy (k) at different heights above ground level. ($u^* = 3$ m/s)



Figure 9: Rate of dissipation of turbulence energy (ϵ) at different heights above ground level. ($u^* = 3$ m/s)

Figures 10 and 11 show the values of k and ϵ for a friction velocity of 6 m/s. By increasing the inlet flow velocity, zones of high turbulence intensity form to the south of the computational domain. This is due to the topography

of this area (Monte de Alba), where large slopes and mountains cause instabilities and flow detachments. High values of k indicate a greater amplitude of velocity field fluctuations, while ε regulates the oscillation frequencies. A higher rate of energy dissipation generates gusts of smaller characteristic length, increasing the frequency of oscillations in the velocity field.

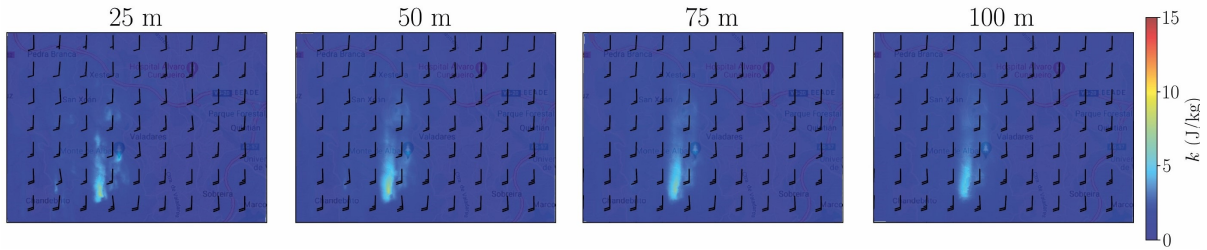


Figure 10: Kinetic turbulence energy (k) at different heights above ground level. ($u^* = 6$ m/s)



Figure 11: Rate of dissipation of turbulence energy (ε) at different heights above ground level. ($u^* = 6$ m/s)

Figures 12 and 13 illustrate the values of k and ε for a friction velocity of 9 m/s. In this configuration, the extension of detachment zones increases, as well as the values of turbulent kinetic energy. This represents a high-turbulence case, posing a significant risk for AAM operations.

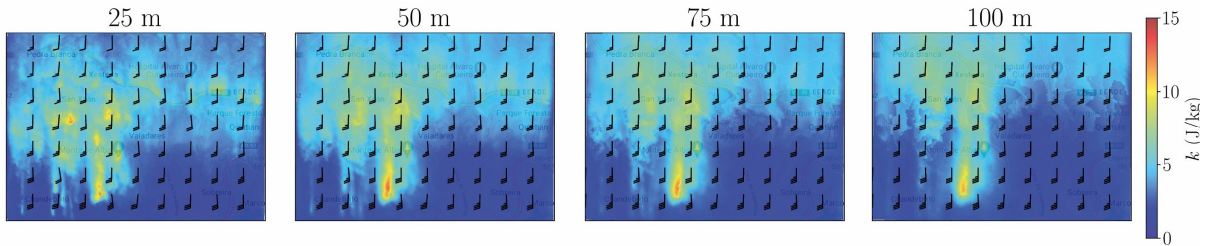


Figure 12: Kinetic turbulence energy (k) at different heights above ground level. ($u^* = 9$ m/s)

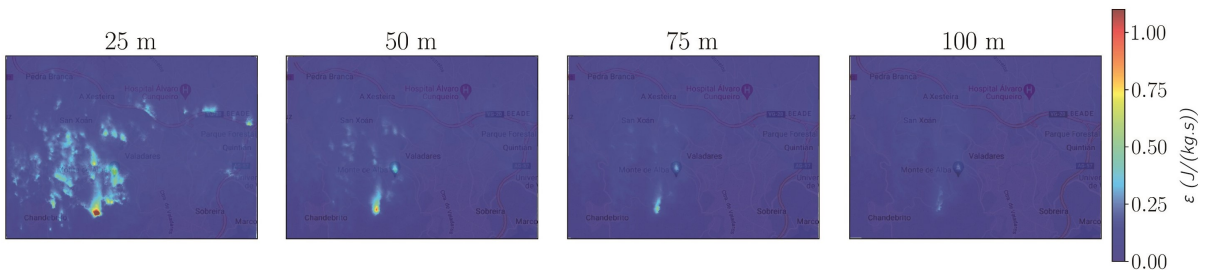


Figure 13: Rate of dissipation of turbulence energy (ε) at different heights above ground level. ($u^* = 9$ m/s)

3.2 Atmospheric turbulence analysis

As observed, the most intense gusts form to the south of the computational domain near the indicated mountainous area in Figure 14. To analyse the wind flow in more detail in this area, a cross-sectional cut of the simulation results is performed.

Figure 15 presents the maps of wind intensity and direction for this cross-sectional terrain for different values of u^* . As can be observed, in all cases, the flow exhibits significant changes in speed and direction due to the

steep topography of the terrain. Behind the mountain peak, the velocity considerably decreases, forming areas of detachment that increase the instability of the wind flow. Figure 16 represents the results of turbulence kinetic energy for the three study cases. For high values of u^* , zones of high turbulence intensity form behind the mountain peak, reaching kinetic energy values of up to 20 J/kg near the surface. In this area, the rate of dissipation ε also reaches the highest values (Figure 17), generating vortices of high intensity and frequency.

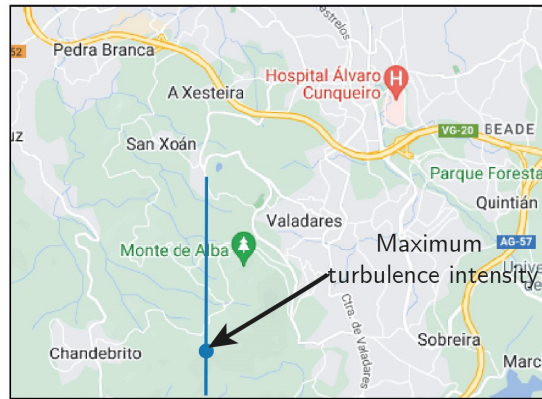


Figure 14: Area of maximum turbulence intensity. Blue line indicates the cross-sectional cut of the zone.

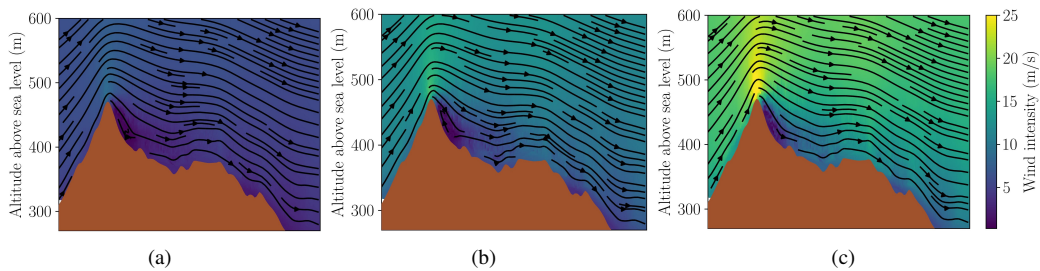


Figure 15: Wind speed maps of the high turbulence intensity region. Brown area represents terrain elevation a) $u^* = 3$ m/s. b) $u^* = 6$ m/s. c) $u^* = 9$ m/s.

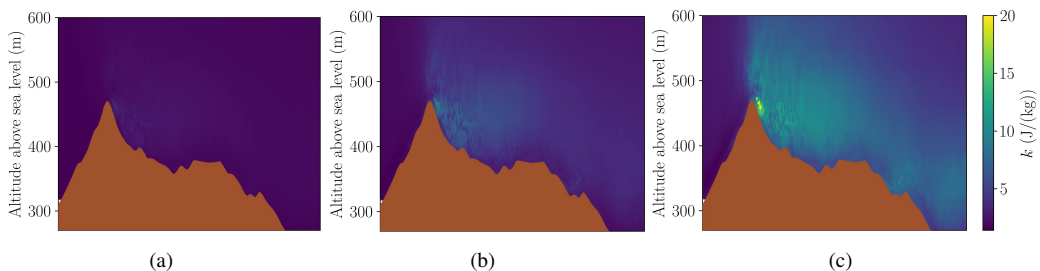


Figure 16: Turbulence kinetic energy (k). Brown area represents terrain elevation a) $u^* = 3$ m/s. b) $u^* = 6$ m/s. c) $u^* = 9$ m/s.

Figures 18, 19, and 20 represent the wind speed fluctuations generated through the Dryden turbulence model at the point of maximum turbulence intensity. To this end, a fixed-wing aircraft with a True Airspeed (v_{TAS}) of 30 m/s. As can be seen, the amplitude of the fluctuations increases with the intensity of the incident wind, reaching oscillation amplitudes of up to 5 m/s for $u^* = 9$ m/s and a flight altitude of 25 m above the ground. This would be a case of very high turbulence intensity that would generate high-frequency oscillations in aerodynamic forces, posing a high risk to operations. By increasing the flight altitude above the ground, the amplitudes of the oscillations decrease as k reduces. Additionally, the PSD of high frequencies also decreases as the rate of dissipation of turbulence energy is lower, resulting in less abrupt fluctuations in the velocity field.

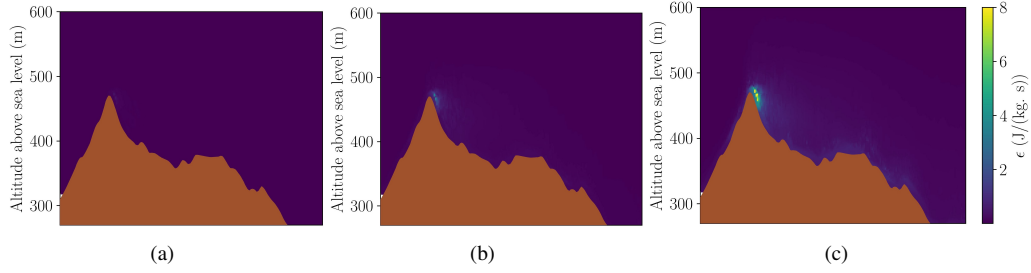


Figure 17: Rate of dissipation of turbulence kinetic energy (ϵ). Brown area represents terrain elevation a) $v^* = 3$ m/s. b) $v^* = 6$ m/s. c) $v^* = 9$ m/s.

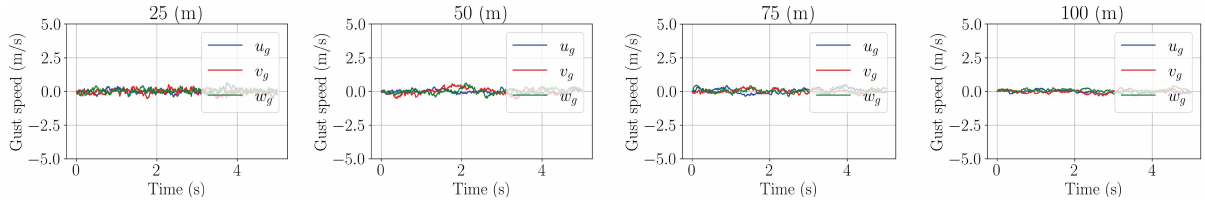


Figure 18: True airspeed fluctuations at different heights above ground level. ($u^* = 3$ m/s, $v_{TAS} = 30$ m/s)

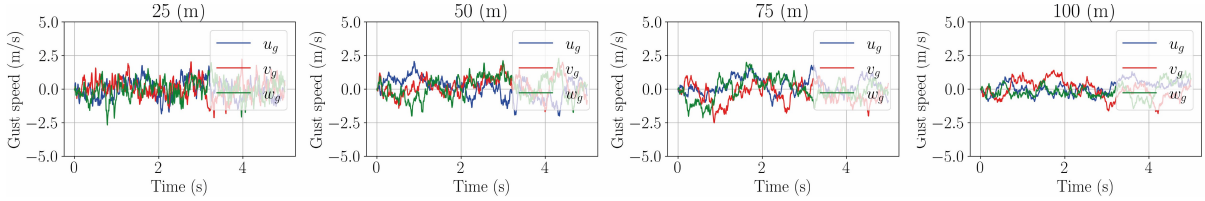


Figure 19: True airspeed fluctuations at different heights above ground level. ($u^* = 6$ m/s, $v_{TAS} = 30$ m/s)

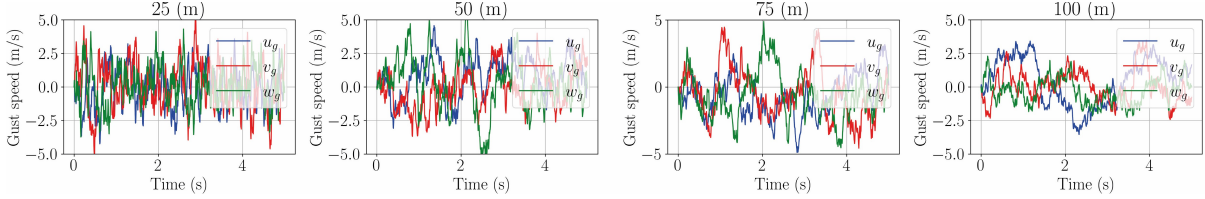


Figure 20: True airspeed fluctuations at different heights above ground level. ($u^* = 9$ m/s, $v_{TAS} = 30$ m/s)

4 Conclusions

This study introduces an automated methodology for the development of high-resolution weather prediction systems for Advanced Air Mobility applications. Using open-source geospatial information, a digital model of an interurban area was created, characterising the physical properties of the different terrain surfaces. From this geometry, a CFD-compatible finite volume mesh was developed, and several simulations were carried out using CFD-software OpenFOAM. Furthermore, an assessment on the impact of wind gusts on AAM operations was carried out using a Dryden turbulence model. Results showed that mountainous areas are prone to create strong wind speed fluctuations, especially in flights close to terrain level.

In future work, the response of different aircraft models to wind gusts will be characterised using more realistic UAV simulators and path planning methodologies will be developed to mitigate the impact of atmospheric turbulence on AAM operations.

ACKNOWLEDGMENTS

Authors would like to acknowledge the funding provided for this work by the Agencia Estatal de Investigación and the European Union - NextGenerationEU, under grant numbers PID2021-125060OB-100 and TED2021-129757B-C3. We also extend our appreciation to Xunta de Galicia for their funding support through the Galician Marine Sciences Program under the Complementary R&D Plan. Additionally, we would like to thank Ministerio de Universidades as they support Enrique Aldao's PhD thesis through grant FPU21/01176

References

- [1] A. P. Cohen, S. A. Shaheen, E. M. Farrar, Urban air mobility: History, ecosystem, market potential, and challenges, *IEEE Transactions on Intelligent Transportation Systems* 22 (9) (2021) 6074–6087. doi:10.1109/TITS.2021.3082767.
- [2] A. Koumoutsidi, I. Pagoni, A. Polydoropoulou, A new mobility era: Stakeholders' insights regarding urban air mobility, *Sustainability* 14 (5) (2022). doi:10.3390/su14053128.
- [3] P. Shiva Prakasha, N. Naeem, P. Ratei, B. Nagel, Aircraft architecture and fleet assessment framework for urban air mobility using a system of systems approach, *Aerospace Science and Technology* 125 (2022) 107072, sI: DICUAM 2021. doi:10.1016/j.ast.2021.107072.
- [4] C. Al Haddad, E. Chaniotakis, A. Straubinger, K. Plötner, C. Antoniou, Factors affecting the adoption and use of urban air mobility, *Transportation Research Part A: Policy and Practice* 132 (2020) 696–712. doi:10.1016/j.tra.2019.12.020.
- [5] A. Straubinger, E. T. Verhoef, H. L. de Groot, Will urban air mobility fly? the efficiency and distributional impacts of uam in different urban spatial structures, *Transportation Research Part C: Emerging Technologies* 127 (2021) 103124. doi:10.1016/j.trc.2021.103124.
- [6] P. S. Yedavalli, E. Onat, X. Peng, R. Sengupta, P. Waddell, V. Bulusu, M. Xue, Assessing the Value of Urban Air Mobility through Metropolitan-Scale Microsimulation: A Case Study of the San Francisco Bay Area, *American Institute of Aeronautics and Astronautics*, 2021, pp. 2021–2338. doi:10.2514/6.2021-2338.
- [7] L. A. Garrow, B. J. German, C. E. Leonard, Urban air mobility: A comprehensive review and comparative analysis with autonomous and electric ground transportation for informing future research, *Transportation Research Part C: Emerging Technologies* 132 (2021) 103377. doi:10.1016/j.trc.2021.103377.
- [8] N. Tepylo, A. Straubinger, J. Laliberte, Public perception of advanced aviation technologies: A review and roadmap to acceptance, *Progress in Aerospace Sciences* 138 (2023) 100899. doi:10.1016/j.paerosci.2023.100899.
- [9] C. Reiche, C. McGillen, J. Siegel, F. Brody, Are we ready to weather urban air mobility (uam)?, in: 2019 Integrated Communications, Navigation and Surveillance Conference (ICNS), 2019, pp. 1–7. doi:10.1109/ICNSURV.2019.8735297.
- [10] C. Reiche, A. P. Cohen, C. Fernando, An initial assessment of the potential weather barriers of urban air mobility, *IEEE Transactions on Intelligent Transportation Systems* 22 (9) (2021) 6018–6027. doi:10.1109/TITS.2020.3048364.
- [11] K. Schweiger, R. Schmitz, F. Knabe, Impact of wind on evtol operations and implications for vertiport airside traffic flows: A case study of hamburg and munich, *Drones* 7 (7) (2023). doi:10.3390/drones7070464.
- [12] M. Steiner, Urban air mobility: Opportunities for the weather community, *Bulletin of the American Meteorological Society* 100 (11) (2019) 2131 – 2133. doi:10.1175/BAMS-D-19-0148.1.
- [13] B. P. Hill, D. DeCarme, M. Metcalfe, C. Griffin, S. Wiggins, C. Metts, B. Bastedo, M. D. Patterson, N. L. Mendonca, *Urban air mobility (uam) vision concept of operations (conops) uam maturity level (uml) – 4*, (Accessed on 12/07/2023) (12 2020).
URL <https://ntrs.nasa.gov/api/citations/20210010443/downloads/UAM%20Vision%20ConOps%20Overview%20Presentation%2018DEC2020.pdf>
- [14] H. K. Ng, *Collaborative weather research and development for urban air mobility*, (Accessed on 12/07/2023) (2022).
URL https://ntrs.nasa.gov/api/citations/20220005500/downloads/20220005500_HokKNg_FPAW2022_presentation_final.pdf
- [15] C. S. B. Grimmond, Progress in measuring and observing the urban atmosphere, *Theoretical and Applied Climatology* 84 (2006) 3–22. doi:10.1007/s00704-005-0140-5.

- [16] Y. Tominaga, L. L. Wang, Z. J. Zhai, T. Stathopoulos, Accuracy of cfd simulations in urban aerodynamics and microclimate: Progress and challenges, *Building and Environment* 243 (2023) 110723. doi:10.1016/j.buildenv.2023.110723.
- [17] T. Ishihara, G.-W. Qian, Y.-H. Qi, Numerical study of turbulent flow fields in urban areas using modified k- ϵ model and large eddy simulation, *Journal of Wind Engineering and Industrial Aerodynamics* 206 (2020) 104333. doi:10.1016/j.jweia.2020.104333.
- [18] D. Hertwig, G. C. Efthimiou, J. G. Bartzis, B. Leitl, Cfd-rans model validation of turbulent flow in a semi-idealized urban canopy, *Journal of Wind Engineering and Industrial Aerodynamics* 111 (2012) 61–72. doi:10.1016/j.jweia.2012.09.003.
- [19] A. Ricci, I. Kalkman, B. Blocken, M. Burlando, M. Repetto, Impact of turbulence models and roughness height in 3d steady rans simulations of wind flow in an urban environment, *Building and Environment* 171 (2020) 106617. doi:10.1016/j.buildenv.2019.106617.
- [20] D. Xiao, C. Heaney, L. Mottet, F. Fang, W. Lin, I. Navon, Y. Guo, O. Matar, A. Robins, C. Pain, A reduced order model for turbulent flows in the urban environment using machine learning, *Building and Environment* 148 (2019) 323–337. doi:10.1016/j.buildenv.2018.10.035.
- [21] A. Y. Deshmukh, M. Davidovic, T. Grenga, R. Lakshmanan, L. Cai, H. Pitsch, A reduced-order model for turbulent reactive sprays in compression ignition engines, *Combustion and Flame* 236 (2022) 111751. doi:10.1016/j.combustflame.2021.111751.
- [22] Z. Wei, Y. Tang, L. Chen, H. Zhang, F. Li, Fast prediction of the performance of the centrifugal pump based on reduced-order model, *Energy Reports* 9 (2023) 51–64, selected papers from 2022 7th International Conference on New Energy and Future Energy Systems. doi:10.1016/j.egy.2023.02.068.
- [23] P. A. Mirzaei, Cfd modeling of micro and urban climates: Problems to be solved in the new decade, *Sustainable Cities and Society* 69 (2021) 102839. doi:10.1016/j.scs.2021.102839.
- [24] I. Paden, C. García-Sánchez, H. Ledoux, Towards automatic reconstruction of 3d city models tailored for urban flow simulations, *Frontiers in Built Environment* 8 (8 2022). doi:10.3389/fbuil.2022.899332.
- [25] J. E. Stoter, [State of the art in 3d city modelling six challenges facing 3d data as a platform](#), *Gym International* (2020).
URL <https://www.gim-international.com/content/article/state-of-the-art-in-3d-city-modelling-2>
- [26] J. Lee, B. Yang, Developing an optimized texture mapping for photorealistic 3d buildings, *Transactions in GIS* 23 (2019) 1–21. doi:10.1111/tgis.12494.
- [27] Berlin Business Location Center, [Berlin 3d - download portal](#), (Accessed on 12/07/2023) (2019).
URL <https://www.businesslocationcenter.de/en/economic-atlas/download-portal>
- [28] T. Kawaguchi, K. Oguni, Automatic conversion of visually consistent digital maps to conforming geometry for computational fluid dynamics, *Journal of Computing in Civil Engineering* 30 (3 2016). doi:10.1061/(ASCE)CP.1943-5487.0000473.
- [29] IGN, Centro de Descargas (CNIG). [http://centrodedescargas.cnig.es/CentroDescargas/catalogo.do? Serie=LIDAR](http://centrodedescargas.cnig.es/CentroDescargas/catalogo.do?Serie=LIDAR) (Last Accessed - 26th December 2023), Online (2023).
- [30] IGN, SIOSE alta resolución. <https://www.siose.es/web/guest/siose-alta-resolucion> (Last Accessed - 26th December 2023), Online (2023).
- [31] Meteogalicia, Histórico de la red meteorológica. <https://www.meteogalicia.gal/observacion/inicio.action> (Last Accessed - 26th December 2023), Online (2023).
- [32] J. Silva, C. Ribeiro, R. Guedes, M.-C. Rua, F. Ulrich, Roughness length classification of corine land cover classes, *Proceedings of EWEC 2007* (01 2007).
- [33] P. Abichandani, D. Lobo, G. Ford, D. Bucci, M. Kam, Wind measurement and simulation techniques in multi-rotor small unmanned aerial vehicles, *IEEE Access* 8 (2020) 54910–54927. doi:10.1109/ACCESS.2020.2977693.